

Topological Optical Spin Injection Beyond Regular Weyl semimetals

Suvendu Ghosh,^{1,*} Chuanchang Zeng,^{2,*} A. Taraphder,¹ Jian-Xin Zhu,^{3,4} and Snehasish Nandy^{5,3,†}

¹*Department of Physics, Indian Institute of Technology Kharagpur, Kharagpur 721302, India*

²*Beijing Academy of Quantum Information Sciences, Beijing, 100193, China*

³*Theoretical Division, Los Alamos National Laboratory, Los Alamos, New Mexico 87545, USA*

⁴*Center for Integrated Nanotechnologies, Los Alamos National Laboratory, Los Alamos, New Mexico 87545, USA*

⁵*Department of Physics, National Institute of Technology Silchar, Assam 788010, India*

Photoinduced effects are now reckoned to be important tools to reveal a rich gamut of entrancing physics in topological materials, which are normally inaccessible via conventional probes. Here we investigate one of these intriguing effects, namely, *optical spin injection* (OSI) beyond the regular Weyl semimetal (WSM), specifically in multi- and higher-order WSMs. Remarkably, we demonstrate that OSI in multi-WSMs can emerge as a frequency-independent quantized response engendered by band linearity and topological charge associated with the node. Interestingly, the frequency independence can be destroyed by going beyond the first-order topological phase where we explicitly show the OSI response is accompanied by peaks for the first-order Weyl nodes while dips for the second-order Weyl nodes. In addition, we elucidate the behavior of OSI in type-II Weyl phases. The predicted signatures of OSI beyond the regular WSM, i.e., multi- and higher-order WSM, could be experimentally exploited, leading us to effectively access as well as distinguish different-order nontrivial Weyl topology.

Introduction— The nontrivial topological properties of three-dimensional Weyl semimetals (WSMs) are embodied by the Weyl nodes, which act as sources or sinks of the Abelian Berry curvature — a momentum space analog of the magnetic field with quantized Berry flux [1–3]. Each Weyl node is associated with a chirality quantum number, known as the topological charge (n), whose strength is related to the Chern number and is quantized in integer values ± 1 [1, 4]. Interestingly, proposals have emerged to realize topological semimetals hosting Weyl nodes with higher topological charges ($n > 1$), specifically referred to as multi-Weyl semimetals (mWSMs) [5–8]. Unlike typical WSMs with linear and isotropic energy dispersion in momenta, mWSMs with $1 < n \leq 3$, constrained by symmetry [6, 8], display naturally anisotropic dispersion. Specifically, the double Weyl semimetal ($n = 2$) and triple Weyl semimetal ($n = 3$) exhibit linear dispersion along one symmetry direction, while demonstrating quadratic and cubic energy dispersion, respectively, along the other two directions.

Recently, based on symmetry and momentum-resolved topological invariants, a novel class of topological phases, dubbed as *higher-order topological phases*, has been proposed to exist in condensed matter systems [9–21]. An p -th order topological phase is characterized by the nonzero higher-order topological invariant - 2^p moment (e.g., quadrupole for $p = 2$) in the bulk and hosts $(d - p)$ dimensional topologically protected states on its edges or corners where d is the dimension of the system [9, 10]. One of the latest additions to this class is *higher-order Weyl semimetal* (HOWSM) [13, 14, 18, 19]. A second-order WSM features at least a pair of second-order Weyl nodes of opposite quantized charge within its bulk, resulting in gapless hinge states with *fractional* charge. Notably, a hybrid-order WSM may also arise, with coexisting first- and second-order nodes in the bulk, thereby giving rise to both hinge states and Fermi arcs on the surface [13, 14].

Weyl semimetals, owing to their unusual band topology,

showcase a variety of fascinating optical phenomena in presence or absence of external fields [1, 22–32]. It has recently been proposed that by activating the spin degrees of freedom, the helical spin-momentum locking of the Weyl node with the combination of chirality can give rise to an interesting nonlinear optical phenomenon: *frequency-independent circular optical spin injection* (OSI) which enables the photo-generation of spin-polarized carriers [33]. The frequency-independent nature and the topological protection of OSI make the regular WSM a very special candidate compared to other systems such as bulk semiconductors and topological insulators [34–38] not only in the field of fundamental interest of probing topology but also in the application in opto-spintronics. Moreover, the spin magnetization generated by the circular OSI can be reversed, without an external magnetic field, only by changing the polarization of light, leading to potential applications in the THz regime.

Therefore, a pressing question arises: What implications does the OSI phenomenon hold beyond regular WSMs, specifically in mWSMs and HOWSMs? Particularly intriguing is the possibility of probing different orders of topological phases in WSMs and discerning them experimentally — an area of profound fundamental interest. This prospect is extremely fascinating because both single-Weyl nodes and second-order Weyl nodes carry a topological charge of *one*, posing a unique challenge to distinguish them. Moreover, it is also fascinating to know whether the frequency-independence of the response persists beyond a regular WSM. Furthermore, can we enhance the OSI response beyond regular WSMs to improve its technological applications? This avenue holds promise for advancing practical implementations of this phenomenon.

In this work, in light of the above questions we investigate circular OSI in mWSMs and HOWSMs using both low-energy and lattice models. Interestingly, we find that the trace of OSI coefficient in mWSM is *independent of the frequency*

of the circularly polarized light (CPL) and *linearly proportional* to the quantized topological charge associated with the node. We reveal these striking features of OSI originate due to the linearity along one direction in the dispersion of mWSMs. This is in sharp contrast with a regular WSM where all three diagonal components remain nonzero. Remarkably, the frequency-independence can be disrupted either by transitioning to the over-tilted nodes or going beyond the first-order topological phase, even within the low-frequency range. We believe the predicted signatures of OSI in this work could serve as a potential diagnostic tool to identify different-order topological phases in experiments and would render a new avenue for contemporary technological applications.

Circular optical spin injection and its general symmetry requirements— The circular OSI, a second-order optical phenomenon, refers to the generation of spin-polarized electrons in the conduction band due to the interband transitions in response to a circularly polarized light (CPL) illumination [34, 39]. These transitions are determined by the optical selection rules and the resulting rate of spin generation can be expressed as [40]

$$\frac{dm_\alpha}{dt} = \gamma_{\alpha\beta}(\omega)[i\mathbf{E}(\omega) \times \mathbf{E}^*(\omega)]_\beta. \quad (1)$$

Here \mathbf{m} is the spin magnetization in the system, α, β indicates the directional component of the spin magnetization and electric field, respectively, and $\gamma_{\alpha\beta}(\omega)$ is the optical spin injection tensor. Clearly, the rate of spin generation is proportional to the light intensity where $\mathbf{E}(\omega)$ is the Fourier component of the electric field at angular frequency ω . Interestingly, the diagonal components of the coefficient ($\gamma_{\alpha\alpha}$) do not need to break any mirror, spatial inversion, or time-reversal symmetry because both \mathbf{m} and $\mathbf{E}(\omega) \times \mathbf{E}^*(\omega)$ (since \mathbf{E} is a polar vector) transform as a pseudovector. Therefore, the trace of $\gamma_{\alpha\beta}$ transforms as a scalar under point group operations.

To calculate the general expression of the diagonal part of the injection coefficient, we first consider the light-electron interaction Hamiltonian as $H_{Ie} = -e\mathbf{v} \cdot \mathbf{A}$ where e is the charge of the electron, \mathbf{A} is the vector potential of the light and \mathbf{v} is velocity operator. We neglect Zeeman coupling with the light field because the Zeeman coupling is found to be weaker than the orbital contribution for typical Dirac and Weyl systems. Considering the second-order response theory within the density matrix formalism on the total Hamiltonian $H = H_0 + H_{Ie}$ with H_0 being the unperturbed Hamiltonian, the general expression of $\gamma_{\alpha\alpha}$ can be written as ($e = \hbar = 1$ for simplicity) [33, 41]

$$\gamma_{\alpha\alpha} = -\frac{\tau g}{8\pi^2} \sum_{l,m} \int d^3k (\Omega_\alpha)_{ml} (\Delta s_\alpha)_{ml} \Delta f_{lm} \delta(\omega_{lm} - \omega), \quad (2)$$

where τ is the relaxation time, g is the g-factor, $\omega_{lm} = \epsilon_l - \epsilon_m$, and $\Delta f_{lm} = f_l - f_m$ with f_l be the Fermi-Dirac distribution function for band l . Here $(\Omega_\alpha)_{ml} = \epsilon_{\alpha\beta\delta} \text{Im}[\langle u_m | i\partial_{k_\beta} | u_l \rangle \langle u_l | i\partial_{k_\delta} | u_m \rangle]$ is the band-resolved Berry

curvature with $|u_l\rangle$ be the periodic part of the Bloch wavefunction and m, l represent the band indices. The spin difference between two bands $(\Delta s_\alpha)_{ml}$ is expressed as $(\Delta s_\alpha)_{ml} = \langle u_m | s_\alpha | u_m \rangle - \langle u_l | s_\alpha | u_l \rangle$. It is important to note that the optical spin injection phenomenon differs from the inverse Faraday effect (IFE) and circular photogalvanic injection (CPGI) current. In IFE, the light-induced magnetization, \mathbf{m} is linearly proportional to the light intensity [42]. On the other hand, in the case of CPGI current, since current J transforms as a polar vector, the finite CPGI current exists only when the inversion is broken, and a material under consideration belongs to one of the gyrotropic point groups. Additionally, the presence of at least one mirror symmetry constrains all the diagonal components of the CPGI coefficient to be zero [43].

Optical spin injection in mWSMs— To study the OSI coefficient $\gamma_{\alpha\beta}$ for mWSM, we consider a generic model with a pair of opposite chirality multi-Weyl nodes with broken inversion and time-reversal symmetries. The corresponding low-energy Hamiltonian of the mWSM can be written as [44–46]

$$\begin{aligned} H_n^s(\mathbf{k}) &= s[\alpha_n k_\perp^n [\cos(n\phi_k)\sigma_x + \sin(n\phi_k)\sigma_y] + v_z(k_z - sQ)\sigma_z] \\ &+ C_s v_z(k_z - sQ) - sQ_0, \end{aligned} \quad (3)$$

where n is the topological charge, $s (= \pm)$ is the valley index or chirality associated with the multi-Weyl node, $k_\perp = \sqrt{k_x^2 + k_y^2}$, and $\phi_k = \arctan(k_y/k_x)$. σ_i 's ($\sigma_x, \sigma_y, \sigma_z$) are the Pauli matrices acting on the mixed spin-orbital basis. Here, v_z and C_s denote the velocity and tilt parameter along the z -direction respectively. Also, $\alpha_n = \frac{v_\perp}{k_0^{n-1}}$, where v_\perp is the effective velocity of the quasiparticles in the plane perpendicular to the z axis and k_0 represents a material-dependent parameter having the dimension of momentum.

The energy dispersion of a multi-Weyl node associated with chirality s is given by $\epsilon_{\mathbf{k},s}^\pm = C_s v_z(k_z - sQ) - sQ_0 \pm \sqrt{\alpha_n^2 k_\perp^{2n} + v_z^2(k_z - sQ)^2}$, where \pm represents conduction (CB) and valence bands (VB) respectively. Clearly, the dispersion around a typical single Weyl node ($n = 1$) is isotropic in all momentum directions for $v_z = v_\perp = v$. On the other hand, for $n = 2$ (3), we find that the dispersion around a double (triple) Weyl node becomes quadratic (cubic) along both k_x and k_y directions whereas varies linearly with k_z . Based on the tilt parameter strength C_s , a Weyl node can be classified as type-I or type-II. Specifically, type-I and type-II (over-tilted) multi-Weyl nodes are characterized by a point-like Fermi surface ($|C_s| < 1$) and finite Fermi pocket ($|C_s| > 1$) at the node [47, 48], respectively. Interestingly, in contrast to a type-I node, a type-II node breaks the Lorentz symmetry [49].

Different Berry curvature components of a multi-Weyl node are given by

$$\Omega_{\mathbf{k},s}^\pm = \pm \frac{s n v_z \alpha_n^2 k_\perp^{2n-2}}{2 \beta_{\mathbf{k},s}^3} \{k_x, k_y, n(k_z - sQ)\}, \quad (4)$$

where $\beta_{\mathbf{k},s} = \sqrt{\alpha_n^2 k_\perp^{2n} + v_z^2(k_z - sQ)^2}$. It is clear from the Eq. (4) that, similar to energy dispersion, the Berry curvature

is isotropic in all momentum directions for a regular Weyl case whereas it becomes anisotropic for WSMs with $n > 1$, i.e., for double WSM ($n = 2$) and triple WSM ($n = 3$).

Having calculated the Berry curvature, we now investigate the OSI response for mWSM. It is important to note that we ignore internode coupling phenomena and apply the approach of independent node approximation [50]. Therefore, the total contribution becomes the sum of the individual contributions from all the nodes. Following Eq. (2), the trace of the OSI response coefficient for a single node with chirality s takes the form

$$\text{Tr}\gamma_{\alpha\beta}^s = -\frac{\tau g}{8n\pi^2} \int d^3k \frac{(\mathbf{\Omega}_{\mathbf{k},s}^+ \cdot \mathbf{v}_{\mathbf{k},s}^+)(\tilde{\mathbf{k}}_s \cdot \mathbf{\Delta}\mathbf{s}_{\mathbf{k},s})}{\epsilon_{\mathbf{k},s}^+ + sQ_0} \delta(\omega_{cv} - \omega),$$

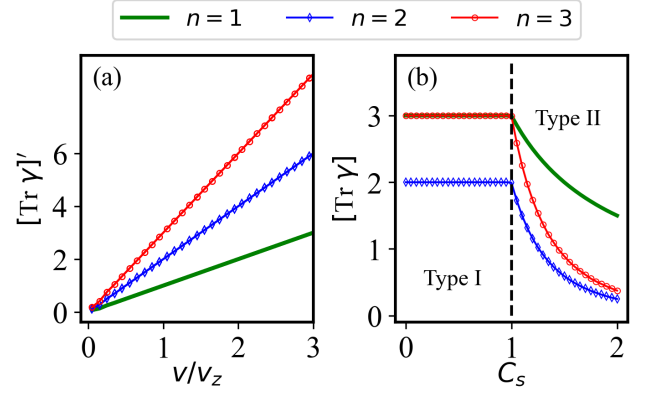
where $\tilde{\mathbf{k}}_s = k_x \hat{\mathbf{x}} + k_y \hat{\mathbf{y}} + n(k_z - sQ) \hat{\mathbf{z}}$. Here $\omega_{cv} = \epsilon_{\mathbf{k},s}^+ - \epsilon_{\mathbf{k},s}^-$ and $\mathbf{\Delta}\mathbf{s}_{\mathbf{k},s} = \frac{s}{\beta_{\mathbf{k}}} [\alpha_n k_{\perp}^n \{\cos n\phi_k \hat{\mathbf{x}} + \sin n\phi_k \hat{\mathbf{y}}\} + v_z(k_z - sQ) \hat{\mathbf{z}}]$ are the energy and spin difference between bands respectively. Since both the Berry curvature ($\mathbf{\Omega}_{\mathbf{k},s}$) and the spin difference ($\mathbf{\Delta}\mathbf{s}_{\mathbf{k}}$) are proportional to the chirality index, the response coefficient $\text{Tr}\gamma_{\alpha\beta}^s$ remains chirality-independent and, consequently, pair-wise contributions do not vanish.

The trace of the OSI coefficient for an inversion and time-reversal symmetry broken type-I mWSM given in Eq. (3) is obtained as [51]

$$\text{Tr}\gamma_{\alpha\beta}^s = -n\gamma_0 \left(\frac{2}{v_{\perp}} \delta_{n,1} + \frac{1}{v_z} \right), \quad (6)$$

where $\gamma_0 = \tau g/12\pi$ and $\delta_{n,1}$ is the Kronecker delta. Equation (6) is one of our main results and has some striking features. *First*, $\text{Tr}\gamma_{\alpha\beta}$ is independent of applied light frequency ω . The frequency independence of OSI has immense potential in opto-spintronics because it does not require fine tuning the light frequency close to resonance. *Second*, the OSI coefficient is linearly proportional to the topological charge n associated with the node. This would have immense importance because it can directly probe the topology of the mWSMs. Hence, the OSI could serve as an important probe to distinguish a regular WSM from an mWSM in the experiment. Additionally, OSI response is increasing with n in mWSM. *Third*, the OSI coefficient is independent of the tilting of the node (particle-hole asymmetry), the time-reversal breaking parameter Q , and the inversion breaking parameter Q_0 ensuring our results are valid for a large class of WSM phases.

To delve into it further, we analytically calculate the response coefficients component-wise and find distinct origins of OSI response in mWSMs compared to a regular WSM. Interestingly, for regular WSM ($n = 1$), all three components of $\gamma_{\alpha\alpha}$, for $\alpha = x, y$ and z , contribute non-vanishingly to the $\text{Tr}\gamma_{\alpha\beta}$ and become equal in an isotropic case ($v_z = v_{\perp} = v$).



(5) FIG. 1. The trace of the OSI response based on the low-energy mWSM model $H_n^s(\mathbf{k})$ as a function of $1/v_z$ and tilt strength C_s in (a) and (b) respectively. Note that $[\text{Tr}\gamma]'$ is normalized by $-\gamma_0$, and a contribution dependent on $2/v_{\perp}$ is subtracted for $n = 1$ in panel (a). As such, we have $[\text{Tr}\gamma(n)]' \propto n/v_z$, consistent with Eq. (6). Panel (b) gives the $[\text{Tr}\gamma]$ profile for different tilt parameters. Obviously, for type-I Weyl nodes, the OSI responses are quantized to integers, while the quantization height decreases with increasing tilt strength in the type-II regime. Here, $C_s = 0.5$ in (a), $v_{\perp} = v_z = v$ in (b), and $\omega = 2v$ is fixed. The other parameters used here are $v = 1, Q = Q_0 = 0, k_0 = 0.8$.

On the other hand, due to an azimuthal (ϕ_k) symmetry in dispersions of mWSMs around k_z -axis, γ_{xx} and γ_{yy} strikingly vanish for multi-Weyl nodes ($n > 1$) and only non-zero contribution comes from γ_{zz} . This is evident from Eq. (6), where $\text{Tr}\gamma_{\alpha\beta}$ for mWSM depends upon v_z only whereas, for regular WSM, it depends upon both v_{\perp} and v_z . This indicates that the OSI response in mWSMs has strong directional dependence. The frequency-independence and linear proportionality with n of OSI response in mWSM appears due to the linearity in dispersion along k_z -direction because the topological charge is associated linearly to the Berry flux monopole only along the direction (i.e., k_z) of linear dispersion of mWSMs. Interestingly, the OSI coefficient is affected by the anisotropic velocity ratio (v_{\perp}/v_z) only in regular WSM as seen from Eq. (6). Therefore, by tuning v_{\perp}/v_z in regular WSM, one can achieve the OSI coefficient to be equal with triple-WSM ($n = 3$) when $v_z = v_{\perp} = v$ and $\tau^{\text{WSM}} = \tau^{\text{mWSM}}$. The above results are also verified by the numerical calculation of the low-energy model as shown in Fig. (1). Going beyond the type-I regime, we have investigated the OSI coefficient for the type-II regime by introducing an energy cutoff $\epsilon_c \sim \hbar v \Lambda_c$, where Λ_c is the corresponding momentum cutoff [52, 53] as shown in Fig. (1)(b). We find that the plateau vanishes in the type-II regime. The model given in Eq. (3) lacks a physical ultraviolet energy cutoff beyond which the low-energy description is no longer valid. Therefore, to verify the robustness of the above results, we calculate the OSI response numerically with a lattice model of mWSM regularized by a physical ultraviolet cutoff and depict its variation with light frequency (ω) and tilt parameter (t_1) in Fig. (2). It can be seen that the

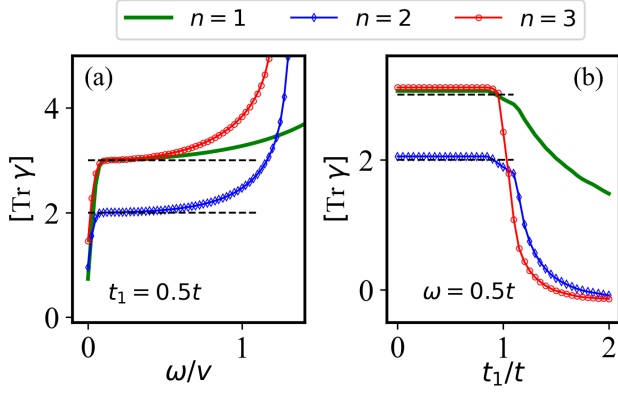


FIG. 2. Numerical results of $Tr[\gamma]$ based on lattice model of mWSM $H_L^n(\mathbf{k})$. Generally, the quantization signature remains present in the lower incident frequency regime, while they deviate gradually with increasing light frequency, attributed to the band regulations. As shown in panel (b), the plateau heights are already slightly above that for the linear Weyl nodes [comparing with Fig. 2(b)] at $\omega = 0.5t$ in the type-I Weyl regime. Here t_1 tune the Weyl node types in $H_L^n(\mathbf{k})$, and $t_1 = 0.5t$ (thus type-I Weyl regime) in panel (a) and $\omega = 0.5t$ in panel (b), as shown in the plot.

plateaus quantized to n can be destroyed in two ways: (i) by going into the high-frequency regime and (ii) by going into the type-II regime. The gradual deviation of $Tr[\gamma]$ beyond a certain ω even for a type-I mWSM is attributed to the fact that with increasing ω , the nonlinearity appears in the band dispersion. On the other hand, only the quantization but not the height quantized to topological charge n can be guaranteed for type-II mWSMs, in contrast to the predictions based on the linearized mWSM. The qualitative differences of the OSI coefficient in type-I and type-II mWSMs can be utilized to distinguish them in the experiment.

Optical spin injection in HOWSM— To enrich our knowledge of the OSI response beyond the first-order topological system, we consider a hybrid-tilt HOWSM given by the lattice model $H^{HW}(\mathbf{k})$ in refs. [13, 14], whose band dispersion is shown in Fig. 3(a). When varying the parameter β in $H^{HW}(\mathbf{k})$, we can achieve regimes with the presence of only the W^i -pair or both the $W^1 + W^2$ pairs Weyl nodes. Interestingly, the corresponding OSI coefficient exhibits an evident transition of a single-peak feature to the double-dip feature, as shown in Fig. 3(b), where ω_p indicates the peak/dip location in frequency space. A few line cuts marked with the corresponding peak/dip locations are given in Fig. 3(c). In such sense, as a proof of concept, we here demonstrate that the above peak-to-dip signature in OSI response might help probe and discern the 1st-order and 2nd-order WSMs in realistic hybrid-order WSM materials, which does not require the calculation of the topological invariants. However, it is

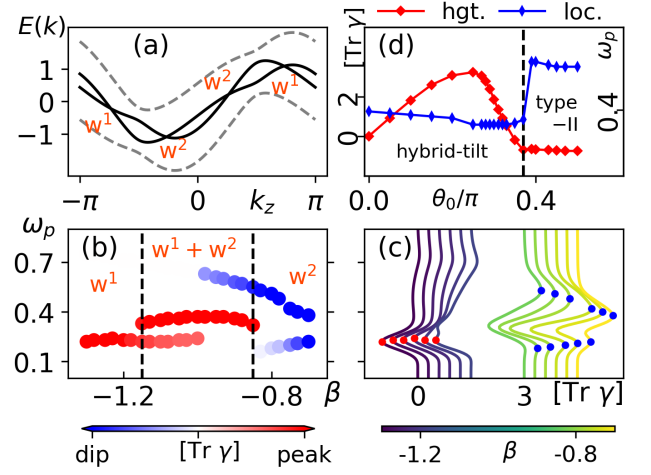


FIG. 3. Panel (a), Band dispersion of the HOWSM based on Hamiltonian $H^{HW}(\mathbf{k})$ [14]. Panel (b) shows the peak(dip) locations in the $\omega - \beta$ parameter space, indicated by color code red (blue) for the response amplitude(height). The dashed lines at $\beta = -1.15, -0.85$ indicate the transition thresholds from the W^1 to the $W^1 + W^2$ phase and from the $W^1 + W^2$ to the W^2 phase, respectively. A few line-cut plots associated with the dip/peak locations are shown in Panel (c), where appropriate offsets are applied. Panel (d) plots the value of $Tr\gamma_{\alpha\beta}^s$ at the peaks, i.e., peak height (peak location), as a function of tuning parameter θ_0 , as given by the red squared line (blue diamond line). The dashed line $\theta_0 \sim 0.36$ indicates the boundary of the hybrid-tilt and type-II phase.

important to note that the linearized model of HOWSM may not be able to capture the distinction of OSI response between first-order and second-order Weyl nodes as the lower-energy behavior are exactly the same for both of them [13, 14]. In addition, we find that both the peak height (dip depth) and peak (dip) location of $Tr\gamma_{\alpha\beta}$ for the HOWSM facilitates the distinction of the hybrid-tilt and type-II only HOWSM phases, as shown in Fig. 3(d) where the parameter θ_0 in $H^{HW}(\mathbf{k})$ can effectively tune the types of W^1 and W^2 .

Discussions— In this paper, we investigate circular OSI in multi- and higher-order semimetals. One of the most remarkable features our work reveals is that the OSI response in a mWSM can exhibit a frequency-independent quantized response, arising from the linearity of bands and the associated topological charge of the node. The frequency-independence would have immense importance in the context of magnetic Weyl systems. This has profound implications, as CPL can reverse magnetization direction swiftly [54], offering a rapid data storage method without requiring precise frequency tuning around a resonance. Our study unveils that the OSI responses in mWSMs are linearly proportional to their respective topological charges (n). This phenomenon could quite remarkably serve as a distinguishing tool for these systems with different topological charges ($n = 2, 3$). Additionally, we discover strong directional dependence in OSI responses, where only γ_{zz} contributes. This is contrary to regular Weyl nodes where all diagonal components remain nonzero.

Remarkably, the frequency-independence can be disrupted either by transitioning to the over-tilted nodes or going beyond the first-order topological phase, even within the low-frequency range. We show that the OSI response is accompanied by peaks for the first-order Weyl nodes while dips for the second-order Weyl nodes. In view of the above discussion, the proposed signatures of OSI response in multi- and higher-order WSM could lead us to effectively access as well as distinguish different-order nontrivial Weyl topology in experiments.

Acknowledgements— S.G. acknowledges the Ministry of Education, India for research fellowship. C.Z. acknowledges support from the NSF of China (Grants No. 12104043). The work at Los Alamos National Laboratory was carried out under the auspices of the US Department of Energy (DOE) National Nuclear Security Administration under Contract No.89233218CNA000001. It was supported by the LANL LDRD Program, and in part by the Center for Integrated Nanotechnologies, a DOE BES user facility, in partnership with the LANL Institutional Computing Program for computational resources.

* Both authors SG and CZ contributed equally.

† snehasish@phy.nits.ac.in

- [1] N. P. Armitage, E. J. Mele, and A. Vishwanath, Weyl and dirac semimetals in three-dimensional solids, *Rev. Mod. Phys.* **90**, 015001 (2018).
- [2] S. Murakami, Phase transition between the quantum spin hall and insulator phases in 3d: emergence of a topological gapless phase, *New Journal of Physics* **9**, 356 (2007).
- [3] A. A. Burkov and L. Balents, Weyl semimetal in a topological insulator multilayer, *Phys. Rev. Lett.* **107**, 127205 (2011).
- [4] D. Xiao, M.-C. Chang, and Q. Niu, Berry phase effects on electronic properties, *Rev. Mod. Phys.* **82**, 1959 (2010).
- [5] G. Xu, H. Weng, Z. Wang, X. Dai, and Z. Fang, Chern semimetal and the quantized anomalous hall effect in HgCr_2Se_4 , *Phys. Rev. Lett.* **107**, 186806 (2011).
- [6] C. Fang, M. J. Gilbert, X. Dai, and B. A. Bernevig, Multi-weyl topological semimetals stabilized by point group symmetry, *Phys. Rev. Lett.* **108**, 266802 (2012).
- [7] S.-M. Huang, S.-Y. Xu, I. Belopolski, C.-C. Lee, G. Chang, T.-R. Chang, B. Wang, N. Alidoust, G. Bian, M. Neupane, D. Sanchez, H. Zheng, H.-T. Jeng, A. Bansil, T. Neupert, H. Lin, and M. Z. Hasan, New type of weyl semimetal with quadratic double weyl fermions, *Proceedings of the National Academy of Sciences* **113**, 1180 (2016).
- [8] B.-J. Yang and N. Nagaosa, Classification of stable three-dimensional dirac semimetals with nontrivial topology, *Nature Communications* **5**, 4898 (2014).
- [9] F. Schindler, A. M. Cook, M. G. Vergniory, Z. Wang, S. S. P. Parkin, B. A. Bernevig, and T. Neupert, Higher-order topological insulators, *Science Advances* **4**, eaat0346 (2018).
- [10] D. Călugăru, V. Juričić, and B. Roy, Higher-order topological phases: A general principle of construction, *Phys. Rev. B* **99**, 041301 (2019).
- [11] B. J. Wieder, Z. Wang, J. Cano, X. Dai, L. M. Schoop, B. Bradlyn, and B. A. Bernevig, Strong and fragile topological dirac semimetals with higher-order fermi arcs, *Nature Communications* **11**, 627 (2020).
- [12] W. Wu, Z.-M. Yu, X. Zhou, Y. X. Zhao, and S. A. Yang, Higher-order dirac fermions in three dimensions, *Phys. Rev. B* **101**, 205134 (2020).
- [13] S. A. A. Ghorashi, T. Li, and T. L. Hughes, Higher-order weyl semimetals, *Phys. Rev. Lett.* **125**, 266804 (2020).
- [14] H.-X. Wang, Z.-K. Lin, B. Jiang, G.-Y. Guo, and J.-H. Jiang, Higher-order weyl semimetals, *Phys. Rev. Lett.* **125**, 146401 (2020).
- [15] L. Zhang, Y. Yang, Z.-K. Lin, P. Qin, Q. Chen, F. Gao, E. Li, J.-H. Jiang, B. Zhang, and H. Chen, Higher-order topological states in surface-wave photonic crystals, *Advanced Science* **7**, 1902724 (2020).
- [16] A. Agarwala, V. Juričić, and B. Roy, Higher-order topological insulators in amorphous solids, *Phys. Rev. Res.* **2**, 012067 (2020).
- [17] R. Noguchi, M. Kobayashi, Z. Jiang, K. Kuroda, T. Takahashi, Z. Xu, D. Lee, M. Hirayama, M. Ochi, T. Shirasawa, P. Zhang, C. Lin, C. Bareille, S. Sakuragi, H. Tanaka, S. Kunisada, K. Kurokawa, K. Yaji, A. Harasawa, V. Kandyba, A. Giampietri, A. Barinov, T. K. Kim, C. Cacho, M. Hashimoto, D. Lu, S. Shin, R. Arita, K. Lai, T. Sasagawa, and T. Kondo, Evidence for a higher-order topological insulator in a three-dimensional material built from van der waals stacking of bismuth-halide chains, *Nature Materials* **20**, 473 (2021).
- [18] L. Luo, H.-X. Wang, Z.-K. Lin, B. Jiang, Y. Wu, F. Li, and J.-H. Jiang, Observation of a phononic higher-order weyl semimetal, *Nature Materials* **20**, 794 (2021).
- [19] Q. Wei, X. Zhang, W. Deng, J. Lu, X. Huang, M. Yan, G. Chen, Z. Liu, and S. Jia, Higher-order topological semimetal in acoustic crystals, *Nature Materials* **20**, 812 (2021).
- [20] B. Xie, H.-X. Wang, X. Zhang, P. Zhan, J.-H. Jiang, M. Lu, and Y. Chen, Higher-order band topology, *Nature Reviews Physics* **3**, 520 (2021).
- [21] Z.-M. Yu, Z. Zhang, G.-B. Liu, W. Wu, X.-P. Li, R.-W. Zhang, S. A. Yang, and Y. Yao, Encyclopedia of emergent particles in three-dimensional crystals, *Science Bulletin* **67**, 375 (2022).
- [22] B. Yan and C. Felser, Topological materials: Weyl semimetals, *Annual Review of Condensed Matter Physics* **8**, 337 (2017).
- [23] S. Nandy and D. A. Pesin, Nonreciprocal optics and magnetotransport in weyl metals as signatures of band topology, *Phys. Rev. B* **106**, L041108 (2022).
- [24] U. Dey, S. Nandy, and A. Taraphder, Dynamic chiral magnetic effect and anisotropic natural optical activity of tilted weyl semimetals, *Scientific Reports* **10**, 2699 (2020).
- [25] B. Sadhukhan and T. Nag, Electronic structure and unconventional nonlinear response in double weyl semimetal SrSi_2 , *Phys. Rev. B* **104**, 245122 (2021).
- [26] J. E. Moore, Optical properties of Weyl semimetals, *National Science Review* **6**, 206 (2018).
- [27] B. Sadhukhan and T. Nag, Role of time reversal symmetry and tilting in circular photogalvanic responses, *Phys. Rev. B* **103**, 144308 (2021).
- [28] C.-K. Chan, N. H. Lindner, G. Refael, and P. A. Lee, Photocurrents in weyl semimetals, *Phys. Rev. B* **95**, 041104 (2017).
- [29] Y. Zhang, H. Ishizuka, J. van den Brink, C. Felser, B. Yan, and N. Nagaosa, Photogalvanic effect in weyl semimetals from first principles, *Phys. Rev. B* **97**, 241118 (2018).
- [30] T. Li, C. Yin, and F. Wu, Giant enhancement of faraday rotation in weyl semimetal assisted by optical tamm state, *Physics Letters A* **437**, 128103 (2022).
- [31] S. Ahn, E. J. Mele, and H. Min, Optical conductivity of multi-weyl semimetals, *Phys. Rev. B* **95**, 161112 (2017).

- [32] P. Goswami, G. Sharma, and S. Tewari, Optical activity as a test for dynamic chiral magnetic effect of weyl semimetals, *Phys. Rev. B* **92**, 161110 (2015).
- [33] Y. Gao, C. Wang, and D. Xiao, Frequency-independent optical spin injection in Weyl semimetals, *SciPost Phys. Core* **7**, 002 (2024).
- [34] I. Žutić, J. Fabian, and S. Das Sarma, Spintronics: Fundamentals and applications, *Rev. Mod. Phys.* **76**, 323 (2004).
- [35] A. Najmaie, R. D. R. Bhat, and J. E. Sipe, All-optical injection and control of spin and electrical currents in quantum wells, *Phys. Rev. B* **68**, 165348 (2003).
- [36] F. Nastos, J. Rioux, M. Strimas-Mackey, B. S. Mendoza, and J. E. Sipe, Full band structure l_{da} and $\mathbf{k} \cdot \mathbf{p}$ calculations of optical spin-injection, *Phys. Rev. B* **76**, 205113 (2007).
- [37] R. A. Muniz and J. E. Sipe, Coherent control of optical injection of spin and currents in topological insulators, *Phys. Rev. B* **89**, 205113 (2014).
- [38] Y. Q. Huang, Y. X. Song, S. M. Wang, I. A. Buyanova, and W. M. Chen, Spin injection and helicity control of surface spin photocurrent in a three dimensional topological insulator, *Nature Communications* **8**, 15401 (2017).
- [39] F. Meier and B. P. Zakharchenya, *Optical Orientation, Modern Problems in Condensed Matter Physics* (North-Holland, Amsterdam, 1984).
- [40] G.-M. Choi, A. Schleife, and D. G. Cahill, Optical-helicity-driven magnetization dynamics in metallic ferromagnets, *Nature Communications* **8**, 15085 (2017).
- [41] Y. Gao, Y. Zhang, and D. Xiao, Tunable layer circular photogalvanic effect in twisted bilayers, *Phys. Rev. Lett.* **124**, 077401 (2020).
- [42] M. Battiato, G. Barbalinardo, and P. M. Oppeneer, Quantum theory of the inverse faraday effect, *Phys. Rev. B* **89**, 014413 (2014).
- [43] F. de Juan, A. G. Grushin, T. Morimoto, and J. E. Moore, Quantized circular photogalvanic effect in weyl semimetals, *Nature Communications* **8**, 15995 (2017).
- [44] X. Li, B. Roy, and S. Das Sarma, Weyl fermions with arbitrary monopoles in magnetic fields: Landau levels, longitudinal magnetotransport, and density-wave ordering, *Phys. Rev. B* **94**, 195144 (2016).
- [45] S. P. Mukherjee and J. P. Carbotte, Doping and tilting on optics in noncentrosymmetric multi-weyl semimetals, *Phys. Rev. B* **97**, 045150 (2018).
- [46] R. M. A. Dantas, F. Peña Benitez, B. Roy, and P. Surówka, Magnetotransport in multi-weyl semimetals: a kinetic theory approach, *Journal of High Energy Physics* **2018**, 69 (2018).
- [47] A. A. Soluyanov, D. Gresch, Z. Wang, Q. Wu, M. Troyer, X. Dai, and B. A. Bernevig, Type-ii weyl semimetals, *Nature* **527**, 495 (2015).
- [48] Y. J. Jin, Y. Xu, Z. J. Chen, and H. Xu, Type-ii quadratic and cubic weyl fermions, *Phys. Rev. B* **105**, 035141 (2022).
- [49] S.-Y. Xu, N. Alidoust, G. Chang, H. Lu, B. Singh, I. Belopolski, D. S. Sanchez, X. Zhang, G. Bian, H. Zheng, M.-A. Husanu, Y. Bian, S.-M. Huang, C.-H. Hsu, T.-R. Chang, H.-T. Jeng, A. Bansil, T. Neupert, V. N. Strocov, H. Lin, S. Jia, and M. Z. Hasan, Discovery of lorentz-violating type ii weyl fermions in laalge, *Science Advances* **3**, e1603266 (2017).
- [50] R. Côté, R. N. Duchesne, G. D. Duchesne, and O. Trépanier, Chiral filtration and faraday rotation in multi-weyl semimetals, *Results in Physics* **54**, 107064 (2023).
- [51] See Supplemental Material for derivations.
- [52] B. Roy, V. Juričić, and S. Das Sarma, Universal optical conductivity of a disordered weyl semimetal, *Scientific Reports* **6**, 32446 (2016).
- [53] S. Ghosh and C. Timm, Charge-spin response and collective excitations in weyl semimetals, *Phys. Rev. B* **99**, 075104 (2019).
- [54] C. D. Stanciu, F. Hansteen, A. V. Kimel, A. Kirilyuk, A. Tsukamoto, A. Itoh, and T. Rasing, All-optical magnetic recording with circularly polarized light, *Phys. Rev. Lett.* **99**, 047601 (2007).